

Formation Dynamics of Quantum Droplets for Homonuclear and Heteronuclear Mixtures

Enrique Calderoli^{1,2,*} and Gerardo Martínez^{1,†}

¹*Instituto de Física, Universidade Federal do Rio Grande do Sul, Porto Alegre-RS, 91501-970, Brasil*

²*Departamento de Psiquiatria, Universidade Federal do Rio Grande do Sul, Porto Alegre-RS, 90035-903, Brasil*

(Dated: January 27, 2026)

Great effort has been invested over the past decade in studying the properties of quantum droplets, a phase of bosonic quantum matter that arises as a consequence of the fluctuating Lee-Huang-Yang correction. However, the dynamics of droplet formation for heteronuclear Bose mixtures is partially understood. Here, we numerically analyze the formation process for homonuclear and heteronuclear boson mixtures in one dimension using a tight-binding model and real-time evolution. A systematic sweep of interaction strengths, mass ratios, and initial conditions allows us to characterize quantitative criteria for droplet formation and equilibration. We find that the energy contribution of the LHY correction dominates the energetic profile of the droplets formed, with the deepest binding occurring for mass ratios $m_2/m_1 \in [1.2, 2.0]$. Breathing oscillations are observed, and the low equilibration rate is consistent with the restricted nature of the phase space for one-dimensional systems; the oscillation frequency is found to have a very weak correlation to the interaction strengths. For the simulation, Gaussian over discrete initial conditions are clearly favorable to the formation of droplets. The results contained herein provide rich insight into the dynamical nature of quantum droplet physics.

I. INTRODUCTION

Petrov's prediction [1] of a new ultracold phase of bosonic quantum matter stabilized by Lee-Huang-Yang (LHY) corrections to the mean-field framework unleashed a torrent of investigations, both theoretical and experimental, about the nature and dynamics of this self-bound state, named quantum droplet, due to its hydrodynamic-like properties. In the past decade, these droplets have been observed in dipolar gases of dysprosium and erbium [2–5], as well as in binary mixtures of potassium isotopes [6–8].

Droplet formation occurs as a result of differences in scaling between the mean-field terms and the LHY corrections. In bosonic 3D systems where droplets are allowed to form, the mean-field terms have different signs (intraspecies being repulsive and interspecies being attractive), mostly canceling each other, with a net effect scaling with $-n^{5/2}$, where n is the local density. The possibility of droplet states arises because the repulsive LHY correction to this system also scales with $n^{5/2}$, compensating the net result of the mean-field terms by creating a local minimum in the system's energy curves and preventing the usual collapse. Interestingly, 1D Bose gases have led to droplet formation with the inverse setup: a net mean-field effect being repulsive and scaling with $n^{3/2}$ and collapse being prevented due to attractive LHY corrections scaling with $-n^{3/2}$ [9]. The particularities of this dimensional crossover have been the topic of many recent and ongoing research efforts [10–12].

Despite the stream of studies on droplet phenomena, many points about this phase, in particular its dynamical properties, have not been adequately addressed. For example, the theoretical formulation of droplets generally assumes homonuclear ($m_1 = m_2$) components, refraining from modeling heteronuclear systems due to the analytic and computational

challenges in dealing with different masses in the Bogoliubov treatment of quantum excitations. Most studies typically employ an approximation of the LHY correction, whose format depends on the specific geometry being studied and is usually taken as some power of n . However, this leaves a large fraction of bosonic systems unaccounted for when it comes to physical models.

Another gap in our understanding of droplet physics is due to most investigations employing imaginary-time evolution techniques, therefore, analyzing these liquid-like states only when equilibrium is reached. Thus, a wealth of physical information about the formation dynamics of quantum droplets remains unexplored.

In this work, we study the real-time formation dynamics of quantum droplets on two-component Bose-Einstein condensates (BECs) on a 1D discrete lattice. We compare how components with different masses ($m_1 \neq m_2$) present distinct behavior from the homonuclear picture, and how different initial states for the system alter the formation and stabilization of the droplets. The remainder of the paper is structured as follows. In Sect. II, we present the model used and the variational method employed based on a Bogoliubov formulation that includes first-order LHY energy corrections, while the implementation details about the numerical scheme is left to the Appendices. The main point here is how to deal numerically with the chemical potential arising from this LHY energy part. In Sect. III, we present the most relevant findings on the dynamical formation of droplets, contrasting how the homonuclear and heteronuclear cases differ. For that, we analyze time formation, energy partitioning, localization, overlapping, breathing modes, and density profiles. We also study, for homonuclear and heteronuclear cases, how the analytical approximations used in the literature perform when compared to the variational approach that we use to compute the chemical potential in the extended Gross-Pitaevskii equations, derived directly from Bogoliubov's theory and whose accuracy is only limited by the error introduced from the numerical integration method. Finally, Sect. IV sets out the conclusions that we can arrive at from the data and analysis of this study.

*Electronic address: enrique.calderoli@gmail.com

†Electronic address: martinez@if.ufrgs.br

II. THEORETICAL FRAMEWORK

The system we study is a two-component Bose mixture in 1D whose Hamiltonian in real-space representation is given by

$$\hat{H} = \int dx \left[\sum_{\sigma=1,2} \hat{\Psi}_\sigma^\dagger(x) \left(-\frac{\hbar^2}{2m_\sigma} \frac{d^2}{dx^2} \right) \hat{\Psi}_\sigma(x) + \sum_{\sigma=1,2} \frac{U_\sigma}{2} \hat{\Psi}_\sigma^\dagger \hat{\Psi}_\sigma^\dagger \hat{\Psi}_\sigma \hat{\Psi}_\sigma + U_{12} \hat{\Psi}_1^\dagger \hat{\Psi}_2^\dagger \hat{\Psi}_1 \hat{\Psi}_2 \right], \quad (1)$$

where $\hat{\Psi}_\sigma(x)$ ($\hat{\Psi}_\sigma^\dagger(x)$) annihilates (creates) a boson of species σ at position x , m_1 (m_2) is the atomic mass for the first (second) condensate, U_1 (U_2) is the intraspecies atomic interaction for the first (second) condensate and U_{12} is the inter-species atomic interaction [13, 14].

This Hamiltonian is a useful model for “quasi-one-dimensional” binary bosonic mixtures, referred to as such because, although they are physically three-dimensional in the laboratory, their dynamics are effectively one-dimensional due to the strong confinement [15, 16] in the transverse directions. This can be achieved through the application of a very tight harmonic trap in two spatial directions, while leaving the third relatively free. When the transverse trapping frequency ω_\perp is sufficiently large so that the associated energy scale $\hbar\omega_\perp$ exceeds the other relevant energies of the system, such as the chemical potential μ , the thermal energy $k_B T$, and the interaction energy, the atoms are frozen in the transverse ground state [17], unable to access the excited transverse modes. As a result, all its relevant dynamics are confined to the axial direction.

The distinction between the condensate phase and the excited states is most easily treated within the context of momentum-space representation, which we adopt from now on. We begin by expressing the field operators on a plane-wave basis in momentum space in the following form:

$$\hat{\Psi}_1(x) = \frac{1}{\sqrt{L}} \left(\hat{a}_0 + \sum_{k \neq 0} e^{ikx} \hat{a}_k \right), \quad (2)$$

$$\hat{\Psi}_2(x) = \frac{1}{\sqrt{L}} \left(\hat{b}_0 + \sum_{k \neq 0} e^{ikx} \hat{b}_k \right), \quad (3)$$

where $k = 2\pi n/L$ with $n \in \mathbb{Z}$ and \hat{a}_k (\hat{b}_k) annihilates a boson of atom species 1 (2) with momentum $\hbar k$ [18]. As such, in both equations above, the first term in parentheses represents the bosons composing the condensate, and the second term represents the bosons at excited states.

The Bogoliubov approximation is based on the assumption that the condensate mode is macroscopically occupied, making \hat{a}_0 and \hat{b}_0 massive compared to the small fluctuations represented by $\hat{a}_{k \neq 0}$ and $\hat{b}_{k \neq 0}$ [18, 19]. Thus, when expanding the expression for the Hamiltonian in momentum representation, one keeps only terms up to quadratic order, which results

in:

$$\hat{H} = \hat{H}^{(0)} + \hat{H}^{(2)} + O(\hat{a}_k^3, \hat{b}_k^3), \quad (4)$$

where $\hat{H}^{(0)}$ contains only condensate operators and $\hat{H}^{(2)}$ is bilinear in the nonzero- k operators and encodes the elementary excitations.

The standard mean-field (MF) treatment consists of neglecting the excited states altogether and equating the condensate mode operators to c -numbers ($\hat{a}_0 \rightarrow \sqrt{N_A}$, $\hat{b}_0 \rightarrow \sqrt{N_B}$), which leads to the MF energy density:

$$\varepsilon_{\text{MF}} = \frac{E_{\text{MF}}}{L} = \frac{1}{2} U_1 n_1^2 + \frac{1}{2} U_2 n_2^2 + U_{12} n_1 n_2, \quad (5)$$

where $n_\sigma = N_\sigma/L$ [20].

Considering that quantum fluctuations only slightly deplete the condensate, the first-order correction to the mean-field treatment is reached when one accounts for the condensate depletion by setting

$$N_1 = \hat{a}_0^\dagger \hat{a}_0 + \sum_{k \neq 0} \hat{a}_k^\dagger \hat{a}_k, \quad (6)$$

$$N_2 = \hat{b}_0^\dagger \hat{b}_0 + \sum_{k \neq 0} \hat{b}_k^\dagger \hat{b}_k, \quad (7)$$

which can be inverted to express the ground-state operators as functions of the operators N_1 and N_2 and of the excited states. After this step, the Hamiltonian becomes a sum over independent $(k, -k)$ sectors.

Defining the Nambu spinor [21] as

$$\Phi^\dagger = (\hat{a}_k^\dagger, \hat{b}_k^\dagger, \hat{a}_{-k}, \hat{b}_{-k}), \quad (8)$$

the quadratic Hamiltonian can be compactly written as

$$\hat{H} = \sum_{k>0} \Phi^\dagger H \Phi + \frac{U_1 N_1^2}{2L} + \frac{U_2 N_2^2}{2L} + \frac{U_{12} N_1 N_2}{L} - \sum_{k>0} \left(\frac{\hbar^2 k^2}{2m_1} + \frac{\hbar^2 k^2}{2m_2} + U_1 n_1 + U_2 n_2 \right). \quad (9)$$

Here, the sum is over $k > 0$ only, as each positive k represents the pair $(k, -k)$. The 4×4 matrix H in Eq. (9) is

$$H = \begin{pmatrix} h_1(k) & h_{12} & U_1 n_1 & h_{12} \\ h_{12} & h_2(k) & h_{12} & U_2 n_2 \\ U_1 n_1 & h_{12} & h_1(k) & h_{12} \\ h_{12} & U_2 n_2 & h_{12} & h_2(k) \end{pmatrix}, \quad (10)$$

where

$$h_\sigma(k) = \frac{\hbar^2 k^2}{2m_\sigma} + U_\sigma n_\sigma, \quad h_{12} = U_{12} \sqrt{n_1 n_2}. \quad (11)$$

Because Φ contains both creation and annihilation operators, diagonalizing the quadratic Hamiltonian is not a standard unitary diagonalization, instead one must solve a Bogoliubov-de

Gennes type eigenproblem. Formally, we introduce the commutation (metric) matrix

$$M_b = [\Phi, \Phi^\dagger] = \begin{pmatrix} I_2 & 0 \\ 0 & -I_2 \end{pmatrix}, \quad (12)$$

and the excitation frequencies ω are obtained [22] by solving the characteristic equation

$$\det(M_b H - \omega I_4) = 0. \quad (13)$$

In this two-component case, the characteristic polynomial reduces to a quadratic equation for ω^2 , which yields two excitation branches:

$$\omega_\pm^2 = \frac{\varepsilon_1^2 + \varepsilon_2^2}{2} \pm \sqrt{\frac{(\varepsilon_1^2 - \varepsilon_2^2)^2}{4} + \frac{U_{12}^2 n_1 n_2 \hbar^4 k^4}{m_1 m_2}}, \quad (14)$$

where

$$\varepsilon_\sigma = \left[\frac{\hbar^2 k^2}{2m_\sigma} \left(\frac{\hbar^2 k^2}{2m_\sigma} + 2U_\sigma n_\sigma \right) \right]^{1/2}. \quad (15)$$

Through a Bogoliubov transformation, the Hamiltonian in Eq. (9) can be rendered into the ground state energy density of the system with the first-order LHY correction included [23]:

$$\begin{aligned} \varepsilon = \frac{E_0}{L} &= \frac{U_1 n_1^2}{2} + \frac{U_2 n_2^2}{2} + U_{12} n_1 n_2 \\ &+ \frac{1}{L} \sum_{k>0} \left(\omega_+ + \omega_- - \frac{\hbar^2 k^2}{2m_1} - \frac{\hbar^2 k^2}{2m_2} - U_1 n_1 - U_2 n_2 \right). \end{aligned} \quad (16)$$

Employing a Euler-Lagrange framework with this energy density leads to the extended Gross-Pitaevskii equations [24, 25] for the system:

$$i\hbar \frac{\partial \Psi_\sigma}{\partial t} = \left(-\frac{\hbar^2}{2m_\sigma} \frac{\partial^2}{\partial x^2} + U_\sigma n_\sigma^2 + U_{12} n_{\sigma' \neq \sigma}^2 + \Delta\mu_\sigma^{\text{LHY}} \right) \Psi_\sigma, \quad (17)$$

where the chemical potential terms due to the LHY correction are obtained from

$$\Delta\mu_\sigma^{\text{LHY}} = \frac{\partial \varepsilon^{\text{LHY}}}{\partial n_\sigma}, \quad (18)$$

with $\sigma = 1, 2$, where ε^{LHY} is the contribution of the LHY correction to the energy density of the ground state of the system as a whole, and is given by the terms inside the summation over the states $k > 0$ in Eq. (16).

To evaluate this sum for this one-dimensional system, we can replace such a discrete sum by an integral in momentum-space, which gives us

$$\varepsilon^{\text{LHY}} = \frac{1}{2\pi} \int_0^{+\infty} \left(\omega_+ + \omega_- - \sum_{i=1,2} \left(\frac{\hbar^2 k^2}{2m_i} + U_i n_i \right) \right) dk. \quad (19)$$

Considering the variational approach used above, we find that the chemical potential contribution due to the LHY correction is given by

$$\Delta\mu_\sigma^{\text{LHY}} = \frac{1}{2\pi} \int_0^{+\infty} \left(\frac{\partial \omega_+}{\partial n_\sigma} + \frac{\partial \omega_-}{\partial n_\sigma} - U_\sigma \right) dk. \quad (20)$$

So far, most studies on quantum droplets have restricted themselves to studying homonuclear ($m_1 = m_2 \equiv m$) mixtures of Bose gases under the single-mode approximation ($n_1 = n_2 \equiv n$) near the threshold $|U_{12}| \approx \sqrt{U_1 U_2}$ [1, 26], which implies $\delta U \equiv U_{12} + \sqrt{U_1 U_2} \approx 0$. In this region, where the LHY correction becomes relevant, droplet formation has been widely demonstrated. We will go far beyond that region.

III. HOMONUCLEAR VERSUS HETERONUCLEAR SYSTEMS

In this Section, we analyze how employing different masses for the species forming condensate 1 and condensate 2 impacts the state and dynamics of the quantum droplets. We also investigate the effect of different initial configurations on the system's behavior and constitution. We do so by numerically integrating the following set of coupled extended Gross-Pitaevskii equations:

$$i\hbar \frac{\partial \Psi}{\partial t} = -\frac{\hbar^2}{2m_1} \frac{\partial^2 \Psi}{\partial x^2} + \left(U_1 |\Psi|^2 + U_{12} |\Phi|^2 + \Delta\mu_1^{\text{LHY}} \right) \Psi, \quad (21)$$

$$i\hbar \frac{\partial \Phi}{\partial t} = -\frac{\hbar^2}{2m_2} \frac{\partial^2 \Phi}{\partial x^2} + \left(U_2 |\Phi|^2 + U_{12} |\Psi|^2 + \Delta\mu_2^{\text{LHY}} \right) \Phi, \quad (22)$$

for a binary Bose mixture in 1D. Here, Ψ represents the wavefunction of the first condensate, with bosons of mass m_1 , while Φ represents the wavefunction of the second condensate, composed of bosonic particles of mass m_2 . We study how this system evolves for a tight-binding model with nearest-neighbor hopping on a discrete lattice of 513 sites, using a variation of the Crank-Nicolson method to solve this coupled set of equations. The units for the results shown below are given in terms of the hopping of the first condensate and use $\hbar = 1$. The integral of Eq. (20) for the chemical potential contributions of the LHY correction to the first and second condensate is computed using the tanh-sinh quadrature. As is common in the literature [27], we neglect the dynamical instabilities that occur from imaginary values for chemical potentials. Details of the numerical implementation can be found in the Appendices A and B.

We consider four types of initial conditions across two modalities: (i) initial shape, with condensates starting out in either a Gaussian configuration or a delta-like configuration, and (ii) initial separation, with condensates departing from the same site on the lattice (no separation), or from distinct sites (variable separation). We study how the variation of these conditions affects the dynamics of the droplets.

A. Formation Time and Equilibrium Time

To classify whether or not a simulation formed a droplet-like structure, we define three criteria: (i) a negative binding energy, which indicates energetic stability against dissociation; (ii) a localized density profile, quantified as a ratio of peak density to average density at the edges of the lattice exceeding a threshold of 10; and (iii) a negative chemical potential in the core region, which is defined as the set of points at which $n > 0.7n_{\text{peak}}$. The formation time t_{form} is therefore the first moment of the simulation in which all three criteria are met.

A second, more stringent test is equilibration. As we study the formation of droplets and neglect dynamical instabilities that may arise from imaginary terms in the chemical potential contributions from the LHY correction, it is to be expected that few of the simulations will actually reach a very steady state of equilibrium. Nevertheless, we define the formed structure to be equilibrated if, in the final 20% of the simulation, it satisfies two more conditions: (i) the oscillation amplitude does not exceed 30% of the mean width, and (ii) the mean width fluctuates by less than 2%.

Figure 1 presents the formation time analysis for homonuclear and heteronuclear systems, as a function of interaction strength variations δU , as well as initial separation.

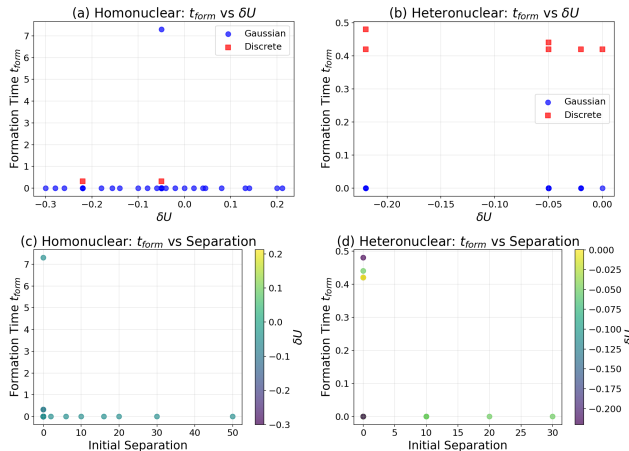


FIG. 1: Formation time analysis. (a,b) Formation time t_{form} versus δU for homonuclear and heteronuclear cases. (c,d) Formation time versus initial separation. Gaussian initial conditions (blue circles) achieve essentially instantaneous formation, while discrete initial conditions (red squares) require $t_{\text{form}} \approx 0.4$ (arbitrary units).

For homonuclear droplets with initial Gaussian conditions, formation is essentially instantaneous with $t_{\text{form}} = 0.0$. This indicates that the smooth Gaussian profiles already satisfy the formation criteria at $t = 0$: the system merely evolves to confirm the sustained nature of the self-bound state. In contrast, runs initialized from discrete (delta-like) occupation exhibit delayed formation with $t_{\text{form}} \approx 0.4$, requiring time for the localized density to redistribute into a smooth droplet profile.

The formation time does not show dependence on the interaction strength for Gaussian initial conditions: all runs

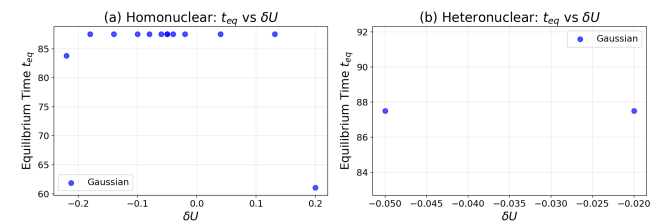


FIG. 2: Equilibration time analysis. (a,b) Equilibration time t_{eq} versus δU showing clustering around $t_{\text{eq}} \approx 87.5$.

achieve instantaneous formation regardless of the value of δU . This uniformity demonstrates that the formation criterion captures initial state preparation rather than dynamical condensation.

Heteronuclear runs exhibit similar behavior: Gaussian initial conditions produce $t_{\text{form}} = 0$, while discrete initialization yields $t_{\text{form}} \approx 0.45$.

When we consider the impact of initial conditions on the success rate of droplet formation, we further establish the importance of the chosen spatial configuration: a total of 97 simulations were attempted, leading to 85 droplets being formed, according to the criteria established above. However, 98.7% (77/78) of the Gaussian initial conditions lead to successful droplet formation, whereas only 42.1% (8/19) of the discrete initial conditions met the formation criteria. This indicates that delta-like initial configurations are somewhat unphysical for modeling structures bound by the LHY correction.

For runs with initially separated components, formation time remains near zero even for initially separated configurations by up to 50 lattice sites [Fig. 1(c,d)]. The coalescence dynamics (Section III D) proceed independently of the formal formation time.

Only 15 of the 85 successfully formed droplets reached the state of equilibrium at the end of the simulation ($t_{\text{max}} = 125$), as defined by the stated criteria. These criteria are deliberately demanding: a droplet can be well-formed and persist indefinitely, yet fail to meet equilibration thresholds if it retains significant collective excitations. The 82.4% of droplets formed that do not equilibrate need not be unstable, as simply maintaining breathing oscillations or slow drifts is sufficient to prevent them from satisfying the stability criteria.

Only 16.7% of the homonuclear droplets formed (9/54) achieve equilibration within the simulated timescale. This rate is comparable to the success rate for the equilibration of the heteronuclear droplets formed: 19.4% (6/31), which indicates that mass asymmetry does not represent a significant factor in relaxation dynamics. The low equilibration rate reflects the persistence of breathing oscillations in 1D systems. Many runs exhibit sustained width variations that, while not growing unboundedly, fail to damp below the 30% amplitude threshold. This is consistent with the theoretical expectations of undamped collective modes in reduced-dimensional systems [11].

If a particular simulation has equilibrated at the end of the simulated timescale, we can define the equilibrium time t_{eq} as the last moment of the simulation in which the width variation

exceeded 2%. Figure 2 presents the analysis of the equilibration time.

All 15 equilibrated simulations have Gaussian initial conditions and no initial separation. 13 represent homonuclear systems and 2 heteronuclear systems. Although the 2 heteronuclear cases that satisfied the equilibrium criteria do not provide great insight, it is interesting that, for homonuclear systems, there is a clustering of equilibration right before $t = 90$, indicating that the width stabilization occurs later in the simulation timescale and the process does not significantly depend on δU .

Although the equilibrium criteria place conditions on the shape dynamics of the formed structures, they place no conditions on its energy. Of the 15 equilibrated runs, only 2 (both homonuclear) have a binding energy that varies by less than 5%.

B. Energy Partitioning and Binding Dynamics

Understanding the energy budget of quantum droplets is essential for identifying the binding mechanism. The total energy of a droplet is the sum of its kinetic energy, due to the hoppings of both condensates, its self-energy, due to the intraspecies interactions of both condensates, its mean-field interaction energy, due to the interspecies interaction, and its LHY energy:

$$E_{\text{total}} = E_{\text{hop}}^{(1)} + E_{\text{hop}}^{(2)} + E_{\text{intra}}^{(1)} + E_{\text{intra}}^{(2)} + E_{\text{inter}} + E_{\text{LHY}} \quad (23)$$

It provides a fundamental characterization of the overall stability of the droplet.

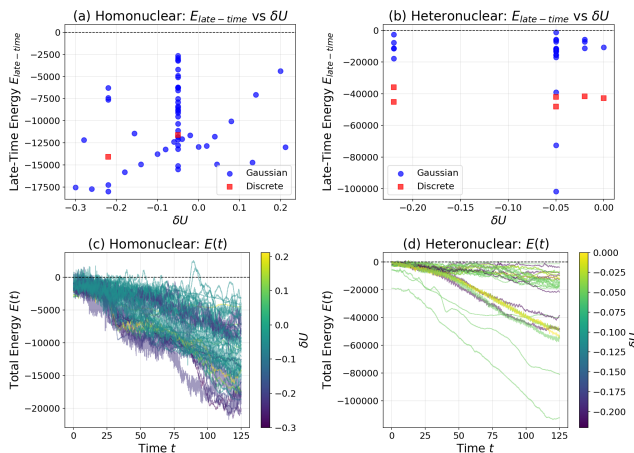


FIG. 3: Late-time energy analysis. (a,b) Late-time energy $E_{\text{late-time}}$ versus δU for homonuclear and heteronuclear cases, showing monotonic deepening with increasingly negative δU . (c,d) Energy time evolution with color indicating δU magnitude.

Fig. 3 provides the energy value analysis of the final configuration of the simulated droplets. We find significant differences in energetics between homonuclear and heteronuclear systems. Heteronuclear droplets achieve significantly

lower energy averages (which correspond to deeper binding, as they are more energetically favorable) than their homonuclear counterparts:

$$E_{\text{late-time}}^{(\text{homo})} = -10,355 \pm 4,188 \quad (24)$$

$$E_{\text{late-time}}^{(\text{hetero})} = -22,445 \pm 22,513 \quad (25)$$

in dimensionless units, where $E_{\text{late-time}}$ indicates the average energy over the last 20% of the simulation. The heteronuclear binding is approximately twice as deep on average, though with substantially larger variance reflecting the strong dependence on the mass ratio. The deeper binding in heteronuclear systems can be understood from the reduced kinetic energy cost when heavier atoms participate in the droplet: the kinetic energy scales as $\hbar^2/(2m)$, so replacing one component with heavier atoms reduces the kinetic energy penalty for localization.

The minimum energy achieved during formation dynamics shows a similar pattern:

$$E_{\text{min}}^{(\text{homo})} = -13,110 \pm 4,636 \quad (26)$$

$$E_{\text{min}}^{(\text{hetero})} = -26,860 \pm 24,979 \quad (27)$$

These minima occur during the initial collapse phase when the density peaks sharply before the system relaxes. The transient minimum represents an overshoot: the system “overshoots” toward deeper binding before collective oscillations and incomplete thermalization cause it to settle at the higher late-time average. The difference $\Delta E = E_{\text{late-time}} - E_{\text{min}} > 0$ quantifies the magnitude of the transient overshoot:

$$\Delta E^{(\text{homo})} = 2,755 \pm 1,303 \quad (28)$$

$$\Delta E^{(\text{hetero})} = 4,415 \pm 3,058 \quad (29)$$

In fractional terms relative to the transient minimum:

$$\left(\frac{\Delta E}{|E_{\text{min}}|} \right)^{(\text{homo})} = 0.223 \pm 0.120 \quad (30)$$

$$\left(\frac{\Delta E}{|E_{\text{min}}|} \right)^{(\text{hetero})} = 0.218 \pm 0.132 \quad (31)$$

Remarkably, both nuclear types show approximately 22% overshoot: the transient minimum is about 22% deeper than where the system ultimately settles. This universal fraction suggests that the overshoot magnitude is determined by generic features of the quench dynamics and the LHY equation of state rather than system-specific parameters. The physical interpretation we provide is as follows: during initial collapse, attractive interactions drive rapid compression, causing the density to peak and the energy to fall to E_{min} . However, this compressed state excites collective modes (primarily breathing) that cannot be fully damped in the near-integrable 1D geometry. The system oscillates around a higher energy $E_{\text{late-time}}$, never returning to the transient minimum. In a fully dissipative system, one would expect $E_{\text{late-time}} \rightarrow E_{\text{min}}$; the persistent 22% gap reflects the weak thermalization characteristic of one-dimensional dynamics.

Within heteronuclear systems, the energy varies dramatically with the mass ratio m_2/m_1 . The deepest binding occurs at intermediate mass ratios ($m_2/m_1 \approx 1.2$), while extreme asymmetries show more moderate binding. This non-monotonic behavior reflects the competition between reduced kinetic energy (favoring heavy atoms) and optimal density matching between components.

For homonuclear droplets, the late-time energy shows a modest correlation with the interaction strength ($r = 0.27$), with stronger attractive interactions ($\delta U < -0.15$) producing deeper binding. For strongly attractive cases, defined as $\delta U < -0.15$, we find $E_{\text{late-time}} = -12,790 \pm 4,499$. For moderately attractive cases with $-0.15 < \delta U < -0.05$, the late-time energy is $E_{\text{late-time}} = -9,005 \pm 3,871$. In near critical cases, for $-0.05 < \delta U < 0.05$, we have $E_{\text{late-time}} = -12,717 \pm 1,221$, and for repulsive cases with $\delta U > 0.05$, $E_{\text{late-time}} = -9,849 \pm 4,224$. Interestingly, near-critical droplets ($\delta U \approx 0$) show binding comparable to strongly attractive cases. This reflects the importance of quantum fluctuations in this regime: the LHY correction provides the dominant stabilization mechanism, leading to robust droplet formation even when the mean-field attraction is weak. Heteronuclear systems show essentially no correlation between δU and late-time energy, with $r = -0.08$, indicating that the effects of mass asymmetry dominate over interaction tuning in determining the energetic structure.

The preparation of the initial state profoundly affects the late-time energy:

$$E_{\text{late-time}}^{(\text{Gaussian})} = -12,648 \pm 13,543 \quad (32)$$

$$E_{\text{late-time}}^{(\text{discrete})} = -35,132 \pm 14,191 \quad (33)$$

Discrete initial conditions produce binding nearly three times deeper than Gaussian preparations. This counterintuitive result arises because discrete states contain substantial high-momentum components that convert to energy during droplet formation. The higher initial kinetic energy allows the system to explore deeper regions of the energy landscape before settling into its final configuration.

Figure 4 shows that initially separated configurations achieve shallower binding than initially co-localized ones. Separated components must first coalesce before experiencing full mutual LHY attraction, resulting in transient positive binding energies during the approach phase. For formed droplets with co-located initial conditions, we find $E_{\text{late-time}} = -14,936 \pm 14,457$ and width $\sigma = 10.2 \pm 10.0$. For initially separated formed droplets, we find $E_{\text{late-time}} = -13,719 \pm 18,947$ and width $\sigma = 22.8 \pm 7.7$. Separated configurations produce wider droplets with comparable binding energy, suggesting that the coalescence process efficiently converts the initial “potential” energy into internal binding.

The relationship between late-time energy and droplet structure differs qualitatively between nuclear types. For homonuclear droplets, the energy shows a weak positive correlation with width ($r = 0.22$): wider droplets have shallower binding, as expected from the reduced density and weaker interactions. Heteronuclear systems show the opposite trend, with strong negative correlation ($r = -0.51$): wider heteronu-

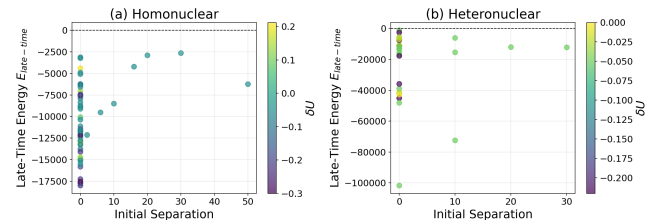


FIG. 4: Late-time energy versus initial separation for (a) homonuclear and (b) heteronuclear droplets.

clear droplets have deeper binding. This counterintuitive behavior reflects the role of mass asymmetry, as heavier atoms naturally spread further because of their lower zero-point energy, and configurations that accommodate this spreading achieve better energetic optimization.

True equilibration would require stability in both width and energetic observables. Our analysis reveals that these criteria are largely independent, and most droplets fail to achieve full equilibration within simulation timescales. Energy stability, defined as $< 5\%$ drift in total energy between successive late-time windows, is achieved by only 7 of the 85 droplets formed, or 8.2%. This is substantially lower than width stability, which occurred for 15 of the 85 formed droplets, or 17.6%, indicating that energy equilibration proceeds more slowly than structural relaxation.

In homonuclear systems, 9.3% of the simulations were energy stable and 24.1% were width stable. For heteronuclear systems, 6.5% were energy stable and 6.5% were width stable. Homonuclear droplets more readily achieve width stability without energy stability, suggesting that breathing mode damping can proceed while slow energy redistribution continues. The joint distribution of the stability criteria reveals four distinct populations. As stated in the previous subsection, only 2 droplets were found to have both stable. 5 droplets were only energy stable and 13 droplets were only width stable. 65 droplets had reached neither kind of stability. The dominance of the “neither stable” category reflects the weak dissipation inherent to one-dimensional systems. The small “both stable” population (2.4% of the formed droplets) represents truly equilibrated droplets that have fully thermalized within simulation time. The asymmetry between “energy stable only” and “width stable only” populations indicates that width stability is more commonly achieved without full energy equilibration. Physically, this suggests that the breathing mode can damp, whereas energy continues to redistribute among other degrees of freedom, such as internal excitations or phonon modes.

Figure 5 presents the analysis of energy partitioning, revealing the central result of this section: complete LHY dominance of the binding budget.

The most striking finding is that $E_{\text{LHY}}/|E_{\text{total}}| \approx 1$ in all $|\delta U|$ values [Fig. 5(b,c)]. Essentially, all binding energy comes from quantum fluctuation corrections; kinetic, self-interaction, and mean-field contributions are negligible. This confirms that quantum fluctuations constitute the essential binding mechanism in 1D droplets, not merely a perturba-

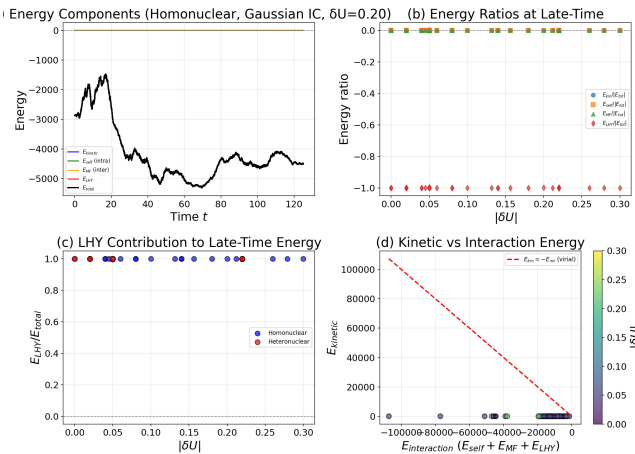


FIG. 5: Energy partitioning analysis. (a) Energy components versus time for a representative run. (b) Energy ratios at late-time versus $|\delta U|$, showing $E_{\text{LHY}}/E_{\text{total}} \approx 1$. (c) LHY fraction of late-time energy. (d) Kinetic versus interaction energy scatter plot.

tive correction.

Figure 6 compares the energy evolution across nuclear configurations and initial conditions.

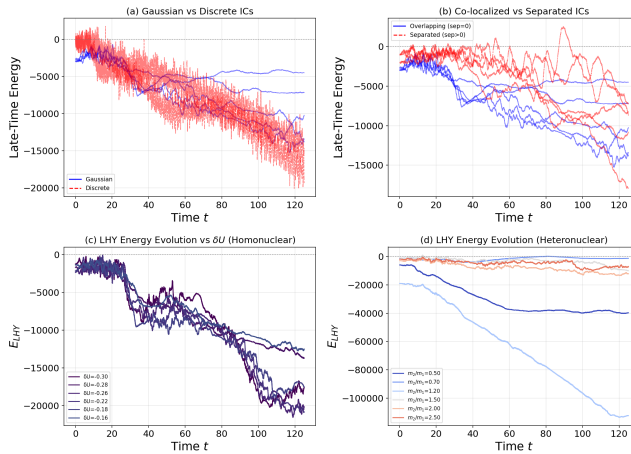


FIG. 6: Energy dynamics comparison. (a) Gaussian versus discrete initial conditions. (b) Co-localized versus separated configurations. (c) LHY energy for homonuclear runs colored by δU . (d) LHY energy for heteronuclear runs colored by mass ratio.

Panel (a) confirms that Gaussian initial conditions lead to stable, oscillatory energy evolution, whereas discrete conditions produce monotonically deepening binding with larger fluctuations. Panel (d) reveals dramatic mass ratio dependence: $m_2/m_1 = 1.2$ achieves extremely deep LHY binding ($E_{\text{LHY}} < -100,000$), while extreme mass ratios ($m_2/m_1 = 0.7$ and $m_2/m_1 = 2.5$) remain much shallower.

Our finding that heteronuclear droplets have a late-time energy twice as negative as that of homonuclear systems could have implications for experimental design. The deeper binding in mass-asymmetric mixtures provides enhanced stability

against thermal fluctuations and three-body losses, potentially extending the observable lifetimes. The non-monotonic dependence of binding on the mass ratio, with optimal binding near $m_2/m_1 \approx 1.2$, suggests that commonly studied mixtures like ³⁹K-⁴¹K (ratio 1.05) may not be optimal to maximize droplet stability. Mixtures with larger mass asymmetry, such as ²³Na-⁸⁷Rb (ratio 3.8), merit investigation.

The low equilibration rates, with only 8.2% of the droplets being energy stable and 17.6% being width stable, reflect fundamental constraints of one-dimensional dynamics. The near-integrability of 1D systems limits thermalization channels, causing droplets to retain collective excitations over timescales much longer than typical experimental windows, a point to which we will return later in this article.

C. Localization Measures: Inverse Participation Ratio and Shannon's Entropy

We employ two complementary measures to quantify the degree of spatial localization of the droplet on the lattice: the inverse participation ratio (IPR) and Shannon's entropy.

The inverse participation ratio is defined as

$$\text{IPR} = \left(\frac{\sum_i |\psi_i|^4}{(\sum_i |\psi_i|^2)^2} \right)^{-1}, \quad (34)$$

summed over all lattice sites. It captures how many sites are effectively occupied by the wave function of the system: IPR ≈ 1 indicates extreme localization; essentially, only one site is occupied by the condensate(s). On the other hand, IPR $\approx N_{\text{sites}}$ indicates complete delocalization; all sites are being equally occupied. For a Gaussian profile of width σ , IPR $\propto \sigma$.

Shannon's entropy is defined as

$$S = - \sum_i p_i \ln p_i, \quad p_i = \frac{|\psi_i|^2}{\sum_j |\psi_j|^2} \quad (35)$$

It is another measure of how “spreads out” the probability distribution of the system. Higher values indicate more delocalization.

Figure 7 presents the localization analysis for homonuclear droplets. As panels 7(a) and 7(b) show, both the IPR and Shannon's entropy display breathing oscillations mirroring width dynamics. For all δU values, the IPR oscillates between a little more than 9 and 18, implying effective localization over 10 to 18 sites. Importantly, IPR shows no secular drift - it oscillates around a stable mean, confirming that the droplets maintain a self-bound character without dispersing or collapsing.

From panel 7(c), we see that the correlation of 0.927 between IPR and width is very strong, indicating that IPR serves as a useful proxy for droplet size independent of the specific profile shape.

Fig. 8 presents the localization measures for heteronuclear droplets. The most interesting conclusion we can reach, from the correlation of 0.637 shown in the panel 8(c), is that IPR

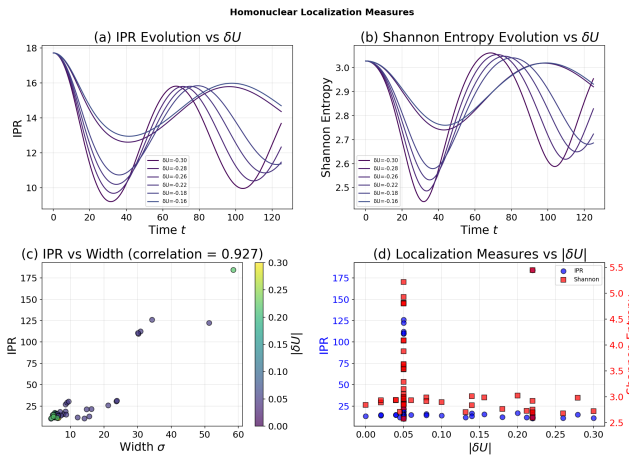


FIG. 7: Localization measures for homonuclear droplets. (a) IPR evolution versus time for different δU values. (b) Shannon entropy evolution. (c) IPR versus width showing a strong correlation of 0.927. (d) Localization measures versus $|\delta U|$ at equilibrium.

does not serve as a good proxy when there is mass-imbalance between atomic species.

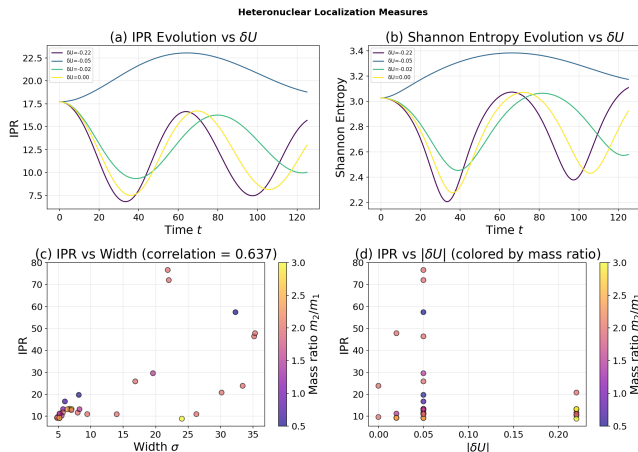


FIG. 8: Localization measures for heteronuclear droplets. (a) IPR evolution versus time for different δU values. (b) Shannon entropy evolution. (c) IPR versus width showing a correlation of 0.637. (d) Localization measures versus $|\delta U|$ at equilibrium.

The peak-to-edge ratio $\mathcal{L} = n_{\text{peak}}/n_{\text{edge}}$, which is one of the metrics used to evaluate droplet formation, shows a great variation between nuclear types: for homonuclear droplets, we have a median $\mathcal{L} \sim 10^7$, while for heteronuclear droplets, we find a median $\mathcal{L} \sim 10^5$. These two orders of magnitude differences reflect the more compact density profiles enabled by symmetric mixtures in homonuclear systems, where both components contribute equally to the central peak density.

It should be noted that initial conditions can have a dramatic effect on the final spatial localization. Gaussian initial states are correlated with compact droplet formations with median $\mathcal{L} \approx 1.3 \times 10^7$, whereas discrete initial configurations lead to

broad structures with median $\mathcal{L} \approx 5.7 \times 10^2$. This may seem paradoxical, as the more localized discrete conditions result in more delocalized states, but we believe it is a manifestation of the uncertainty principle: the extreme initial localization (with a very small spatial uncertainty) must have a correspondingly large momentum uncertainty. This range of momentum states, and its accompanying kinetic energy, must be accommodated as the system relaxes to an equilibrium stabilized by the LHY correction.

D. Component Overlap and Coalescence Dynamics

For two-component droplets to achieve their maximal binding energy, the two species must overlap spatially. We characterize this through the normalized overlap integral:

$$\mathcal{O}(t) = \frac{\int dx |\psi(x, t)|^2 |\phi(x, t)|^2}{\sqrt{\int dx |\psi|^4 \int dx |\phi|^4}} \quad (36)$$

which equals unity for perfectly overlapping distributions and zero for completely separated components.

Figure 9 presents the overlap analysis. By analyzing panel 9(a), we can see that systems with separated initial conditions have overlap increase from near zero to near unity over timescales that depend on the initial separation. The coalescence dynamics shows clear sigmoidal behaviors, with a slow initial approach, a rapid merging, and stabilization at high values of \mathcal{O} . For an initial separation of 2 sites, we achieve $\mathcal{O} \approx 0.98$ by $t \approx 10$. For condensates initially 10 sites apart, we reach $\mathcal{O} \approx 0.9$ by $t \approx 20$. The oscillations displayed over time indicate that the dynamics of capture of initially separated condensates is not monotonic. However, it is clear that the sheer initial separation plays a limited role in the evolution of coalescence, as systems with equal initial separation, such as the case of separations of 20 sites initially, can reach $\mathcal{O} > 0.8$ in either $t = 60$ or $t = 120$. The determination will be made by other parameters.

The panel 9(b) shows that most of the values of $|\delta U|$ used are sufficient to guarantee near-perfect coalescence ($\mathcal{O} > 0.95$) for both homonuclear and heteronuclear systems. The exceptions occur for very small values of $|\delta U|$, where the attraction between components provides insufficient driving force for the capture of both condensates into a single structure to occur.

We can see from 9(c) that there is a systematic decrease in the final overlap reached with increased initial separation: zero separation maintains $\mathcal{O} \approx 1.0$; separations up to 20 sites achieve $\mathcal{O} > 0.8$; beyond 30 sites, overlap drops to below $\mathcal{O} \sim 0.4$. This relationship is largely independent of $|\delta U|$, being dominated by geometric constraints and limitations of the simulated time scale.

Remarkably, 9(d) shows that the final overlap has essentially no dependence on the mass ratio. Almost all heteronuclear mixtures, for m_2/m_1 varying between 0.5 and 3.0, reach $\mathcal{O} > 0.95$, showing that the coalescence dynamics is robust against kinetic energy differences.

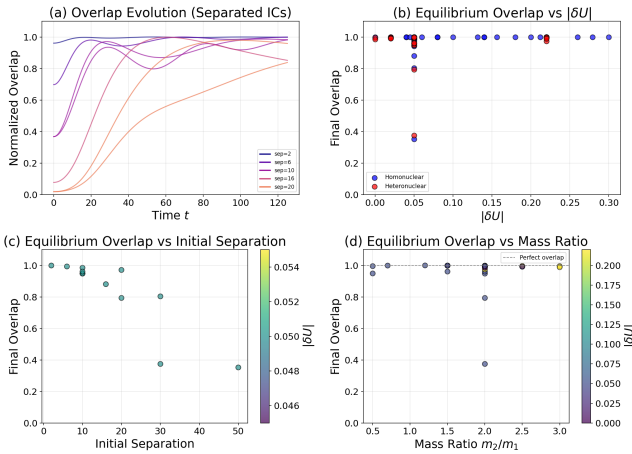


FIG. 9: Component overlap and miscibility. (a) Overlap evolution for runs with different initial separations. (b) Final overlap versus $|\delta U|$. (c) Final overlap versus initial separation. (d) Final overlap versus mass ratio.

The high final overlaps indicate the droplet state is miscible - both components occupy the same region rather than phase-separating. This is expected, as the attractive inter-component interaction ($U_{12} < 0$) favors overlap, and the LHY correction further stabilizes the mixed configuration.

E. Breathing Mode Analysis

In the context of droplet physics, the term “breathing” refers to coherent oscillations in the width of the core fraction of the system that is identified as the droplet. It is the lowest-lying form of collective excitation for our system. In 1D, it is important to remember that the overall topology of the corresponding phase space is quite restricted, and hence there are limited mechanisms for dissipation of energy and momentum. Nevertheless, the dynamics of this Bose mixture, especially at the droplet-forming threshold, can still be very rich.

Figure 10 presents the equilibrium width analysis, contrasting homonuclear (panels (a) and (c)) and heteronuclear systems (panels (b) and (d)).

It is clear, therefore, that both homonuclear and heteronuclear droplets exhibit an interesting bimodal distribution of equilibrium widths, with most forming compact structures and a few more extended outliers. These cases of larger widths largely represent either discrete initial conditions or initial separation, for which the component clouds merge into an elongated formation rather than a compact droplet. In particular, note that the dependence on δU is generally weak: compact formations that represent one of these modes are essentially independent of the interaction strength, while wider structures do not obey a clear trend.

Figure 11 presents the analysis of the breathing mode. We extract the breathing frequency using the Fast Fourier Transform (FFT) analysis of the time series of width $\sigma(t)$ after linear detrending. To avoid spurious detection of slow drift, we

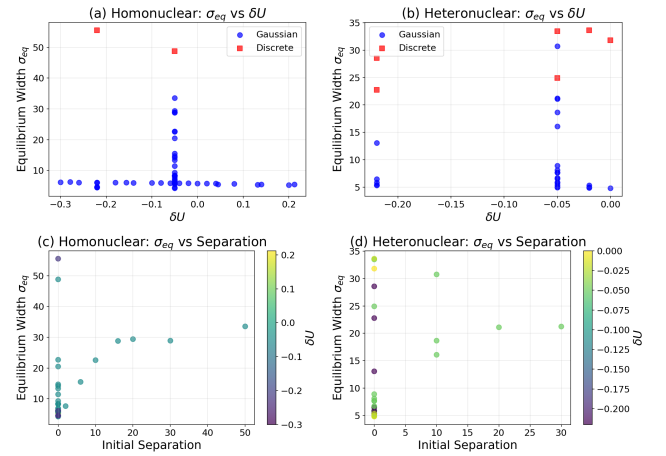


FIG. 10: Equilibrium width analysis. (a,b) Equilibrium width σ_{eq} versus δU for homonuclear and heteronuclear cases. (c,d) Equilibrium width versus initial separation.

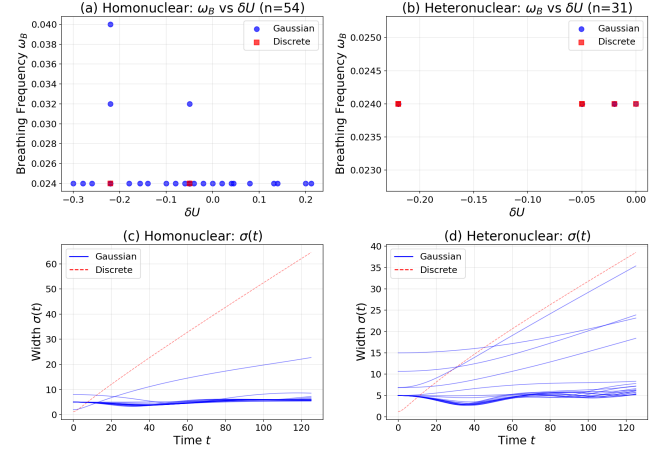


FIG. 11: Breathing mode analysis. (a,b) Breathing frequency ω_B versus δU for homonuclear and heteronuclear cases. (c,d) Width time series $\sigma(t)$ showing persistent oscillations.

impose a frequency floor $f_{min} = 2/T$, where T is the period of oscillation, thereby requiring at least 2 complete oscillations. Peak detection requires a Signal-to-Noise Ratio (SNR) greater than 10 relative to the spectral mean. We obtain valid breathing frequencies for all 85 simulations classified as having formed a droplet.

Of the 85 cases, 82 are found to have a breathing frequency of $\omega_B = 0.0240$, including all heteronuclear droplets and 51 (out of 54) homonuclear droplets. Two homonuclear droplets have a frequency $\omega_B = 0.032$, and one homonuclear droplet has a frequency $\omega_B = 0.040$. These higher frequencies appear preferentially for strong interactions ($\delta U < -0.15$), where the droplet is more tightly bound. This suggests that these values, which we note as being quantized, correspond to excitations of higher breathing modes when sufficient energy is available. As all heteronuclear droplets had the same frequency, we conclude that the frequency is independent of the

mass ratio m_2/m_1 .

Panels 11(c) and 11(d) show that Gaussian initial conditions lead to clean sinusoidal oscillations without any sign of amplitude decay over the simulated period, whereas discrete initial conditions have more complex dynamics, exhibiting superimposed fluctuations unrelated to droplet dynamics or monotonically increasing width, which represent cases of failed droplet formation.

Figure 12 presents the damping rate analysis for homonuclear and heteronuclear droplets. We computed the damping rate from the envelope of detrended width oscillations using the Hilbert transform analysis. The envelope is fit to exponential decay $A(t) = A_0 e^{-\gamma t}$ to extract the damping rate γ .

Damping of breathing oscillations proceeds through coupling to other degrees of freedom and eventual thermalization. We extract valid damping rates for 69 of the 85 formed droplets. The extraction of the damping rate failed for 16 runs, predominantly homonuclear configurations (15/16). Analysis reveals that these failures correlate with low breathing amplitude: runs with invalid damping exhibit mean amplitude 0.098 ± 0.073 , compared to 0.246 ± 0.133 for successful extractions. The Hilbert transform envelope method requires measurable amplitude decay to fit an exponential; when oscillations are small (amplitude $\lesssim 10\%$), the envelope becomes essentially flat, yielding fitted decay rates indistinguishable from zero or slightly negative. Indeed, 6 of the 16 failed runs are classified as equilibrated, where stable width by definition precludes observable damping. Rather than report potentially spurious values, we conservatively exclude these runs from damping statistics. This limitation does not affect our physical conclusions, as the failed runs represent droplets that have reached equilibrium or exhibit oscillations too weak for reliable damping measurement.

The overall damping rate is found to be

$$\gamma = 0.0064 \pm 0.0047 \quad (37)$$

in dimensionless units, which corresponds to characteristic damping timescales of

$$\tau_{\text{homonuclear}} = 1/\gamma_{\text{homonuclear}} \approx 168, \quad (38)$$

$$\tau_{\text{heteronuclear}} = 1/\gamma_{\text{heteronuclear}} \approx 142. \quad (39)$$

As these timescales exceed the simulated time of $T = 125$, it is easy to see why most droplets do not equilibrate.

As stated in the beginning of this Section, the theoretical expectation in 1D would be $\gamma \rightarrow 0$, as breathing modes lack an effective way to couple to other excitations when the only channels for momentum transfer are backward and forward.

Another relevant characterization is the breathing amplitude, the width fraction that actually varies during the oscillation. For homonuclear droplets, the mean amplitude fraction was $\langle A \rangle = 0.191 \pm 0.143$. For heteronuclear droplets, the mean amplitude was $\langle A \rangle = 0.265 \pm 0.111$. This higher mean amplitude fraction for oscillations of heteronuclear droplets may reflect the additional degree of freedom of these kinds of systems - the relative motion between the two components with different masses - which may store oscillatory energy.

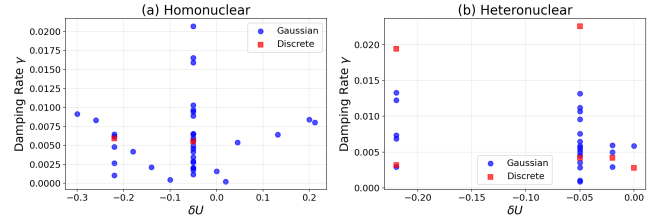


FIG. 12: Damping rate versus δU for (a) homonuclear and (b) heteronuclear droplets.

F. Density Profile Characterization

In Figure 13, we can see the evolution of the density profile for a set of representative cases. Upon reaching equilibrium, three analytical forms were fitted to every droplet: Gaussian $n(x) = n_0 \exp[-(x - x_0)^2/2w^2]$, super-Gaussian $n(x) = n_0 \exp[-(x - x_0)^4/w^4]$, and sech^2 as $n(x) = n_0 \text{sech}^2[(x - x_0)/w]$. Of the 85 droplets formed, 45 were best fitted by the sech^2 function, while 40 were best fitted by the Super-Gaussian. We notice a significant difference in the fitting preference between nuclear types: 55.6% of homonuclear droplets were best suited by Super-Gaussian, while 67.7% of heteronuclear droplets were best suited by sech^2 . No case was best fitted by the Gaussian profile.

As was already shown in one-dimension [11], the flat profile that has been extensively characterized in quantum droplets is controlled by the flatness parameter $\gamma \propto \delta U N^{2/3}$, and only appears for large $\gamma > 0$. Computing this parameter $\delta U N^{2/3}$ for the region of the parameter space we explored in these simulations, we see that these values are very small, indicating that a flat-top profile is very unlikely to appear here.

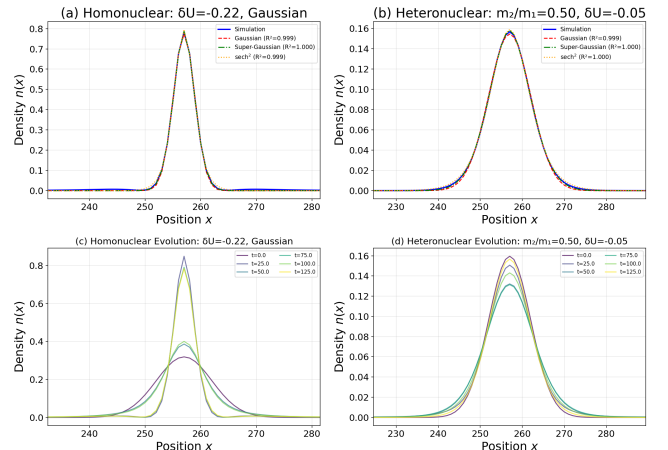


FIG. 13: Density profile fits. (a,b) Equilibrium profiles with Gaussian, super-Gaussian, and sech^2 fits for homonuclear and heteronuclear cases. (c,d) Some profile evolution showing time snapshots.

In Fig. 14, we present the time evolution of the density profile for two homonuclear simulations; one of them was best fitted by a Super-Gaussian function, and the other best fitted

by the sech^2 function. Fig. 15 presents the equivalent figures for heteronuclear droplets.

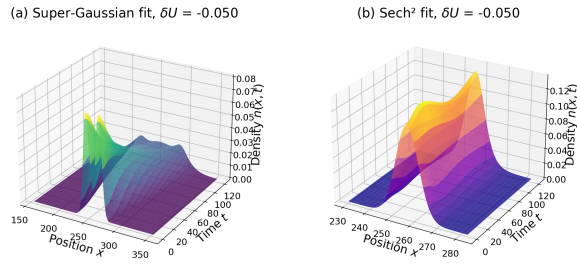


FIG. 14: Time evolution of the density profile for homonuclear droplets for a simulation best fitted by a (a) Super-Gaussian function and by a (b) sech^2 function.

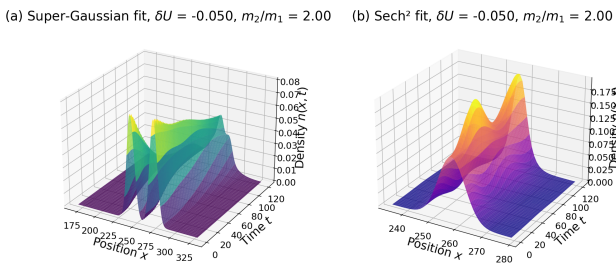


FIG. 15: Time evolution of the density profile for heteronuclear droplets for a simulation best fitted by a (a) Super-Gaussian function and by a (b) sech^2 function.

IV. CONCLUSIONS

We have studied systematically domain formation using real time evolution of quantum droplets in two-component Bose mixtures in one dimension. We integrated an extended version of the Gross-Pitaevskii equations, derived from a Bogoliubov formalism that includes a Lee-Huang-Yang (LHY) first-order correction in energy. We explicitly integrate their k -space integral expressions, which vary implicitly in space and time at each step of integration, as given from Eq. (20).

Our aim in this work was to compare homonuclear systems from heteronuclear systems in a statistical approach by measuring many parameters from its dynamic evolution for different interaction strengths, mass-imbalance and initial conditions. We imposed severe restrictions on the identification of droplet-like structures, such as formation time and equilibration, for Gaussian and discrete initial conditions. From there on, we started to identify the binding mechanism by comparing the energy partitioning of accepted droplets for homonuclear and heteronuclear cases. The most remarkable result here is that LHY contributions dominate the binding budget in most of the situations. Another feature relates the late-time binding energy preference to mass-imbalanced systems,

which is a strong indicative for experimentalists. The very low rate of equilibration is a reflection of the limited decay channels in 1D dynamics.

Furthermore, localization aspects measured from the IPR and Shannon entropy clearly separate homonuclear from heteronuclear behavior, with shallow/deep binding energies, respectively. On the other hand, initial conditions may have dramatic effects in localization, where discrete initial configurations lead to broader structures as compared to Gaussian initial conditions, which we ascribe to the uncertainty principle: extreme initial conditions have larger momentum uncertainty, consequently, a broader accompanying kinetic energy to equilibrate the final configurations stabilized by the LHY correction.

The coalescence aspects are revealed to be independent of the mass-imbalance (namely, on kinetic energy differences) but quite dependent on the initial separation (for rather obvious reasons). No clear dependence of the overlap of the two components on the interaction strength was revealed, except for very small values of δU .

Finally, breathing modes were detected even for such small integration times in our scheme (at least, 2 complete oscillations were detected overall). For the accepted droplet cases and for Gaussian initial conditions, a fixed value for the breathing frequency was found for most cases, indicating independence in the mass ratios and interaction strengths. Importantly, these breathing modes are very atypical coherent oscillations from collective excitations of our system.

In concluding this report, we may say that most of the droplets formed were best fitted with functions known for generating flat-top profiles in other regions of the parameter space. We present two cases of time evolution in figures 14 and 15, which are not very representative of our results. Both were fitted with sech^2 and Super-Gaussian functions, which support various forms already published for quantum droplets in [11].

ACKNOWLEDGMENTS

The authors thank Sandra D. Prado, Sergio G. Magalhães, and Marcos S. Figueira da Silva for many insightful comments. Simulations were performed on 4th Generation Intel Xeon Scalable processors provided by Amazon Web Services (AWS) in São Paulo (Brasil) through the EC2 platform, using the x86-64 architecture.

Appendix A: Tight-binding model and Crank-Nicolson scheme

In Sect. II we presented the continuous version of extended Gross-Pitaevskii equations that govern the dynamics of the system studied in this paper. In this Appendix, we present the choice of discretization used for numerical integration and the algorithm chosen for the task. We use a 1D tight-binding model whose time evolution is described by

$$i\hbar \frac{\psi_i^{n+1} - \psi_i^n}{\Delta t} = -J_1 (\psi_{i+1}^n + \psi_{i-1}^n) + (U_1 |\psi_i^n|^2 + U_{12} |\phi_i^n|^2 + \Delta\mu_1^{\text{LHY}}|_i^n) \psi_i^n, \quad (\text{A1})$$

$$i\hbar \frac{\phi_i^{n+1} - \phi_i^n}{\Delta t} = -J_2 (\phi_{i+1}^n + \phi_{i-1}^n) + (U_2 |\phi_i^n|^2 + U_{12} |\psi_i^n|^2 + \Delta\mu_2^{\text{LHY}}|_i^n) \phi_i^n, \quad (\text{A2})$$

where ψ_i^n (ϕ_i^n) is the Wannier wavefunction for the first (second) condensate on the i -th lattice site at the n -th timestep. J_1 and J_2 denote the hopping terms for the first and second condensates, respectively. $\Delta\mu_1^{\text{LHY}}|_i^n$ is the chemical potential contribution due to the LHY correction for the first condensate, evaluated numerically at the site i and at time n . Similarly, $\Delta\mu_2^{\text{LHY}}|_i^n$ represents the same for the second condensate.

Equations (A1) and (A2) are integrated using a variant of the Crank-Nicolson scheme [28, 29]. The standard Crank-Nicolson method for the Schrödinger equation [30, 31] averages the right-hand side at times t_n and t_{n+1} :

$$i\hbar \frac{\psi_i^{n+1} - \psi_i^n}{\Delta t} = \frac{1}{2} \sum_{k=1}^{N_{\text{sit}}} (H_{ik}^{(1),n+1} \psi_k^{n+1} + H_{ik}^{(1),n} \psi_k^n), \quad (\text{A3})$$

for the first condensate and, equivalently, for the second condensate. Here, the effective single-particle Hamiltonian for the first condensate is

$$H_{ik}^{(1),n} = -J_1 (\delta_{i,k+1} + \delta_{i,k-1}) + V_{\text{eff},i}^{(1),n} \delta_{ik}, \quad (\text{A4})$$

with the effective on-site potential

$$V_{\text{eff},i}^{(1),n} = U_1 |\psi_i^n|^2 + U_{12} |\phi_i^n|^2 + \Delta\mu_1^{\text{LHY}}|_i^n. \quad (\text{A5})$$

The effective potential $V_{\text{eff},i}^{(1)}$ (and therefore the effective Hamiltonian $H^{(1)}$) depends on time through the local densities $n_{1,i}(t) = |\psi_i(t)|^2$ and $n_{2,i}(t) = |\phi_i(t)|^2$.

A fully implicit Crank-Nicolson scheme as in Eq. (A3) would require evaluating $H^{n+1} = H(|\psi^{n+1}|^2, |\phi^{n+1}|^2)$, but ψ^{n+1} is the unknown for which we are solving. This creates a nonlinear system that must be solved iteratively at each timestep, significantly increasing the computational cost. To avoid this overhead, we adopt a semi-implicit approach, also known as lagged nonlinearity [32]: the effective potential is evaluated entirely at the current time t_n , yielding the scheme

$$i\hbar \frac{\psi_i^{n+1} - \psi_i^n}{\Delta t} = \frac{1}{2} \sum_k H_{ik}^n (\psi_k^{n+1} + \psi_k^n), \quad (\text{A6})$$

where $H^n \equiv H(|\psi^n|^2, |\phi^n|^2)$. This can be rewritten in matrix form as

$$\left[I + \frac{i\Delta t}{2\hbar} H^n \right] \psi^{n+1} = \left[I - \frac{i\Delta t}{2\hbar} H^n \right] \psi^n. \quad (\text{A7})$$

Since H^n is known from the previous timestep, this is a linear tridiagonal system, which we solve by the Thomas algorithm [33, 34]. The same treatment is applied to the second condensate.

We now derive explicitly the truncation error introduced by the semi-implicit approximation. The right-hand side of Eq. (A6) is

$$\frac{1}{2} H^n (\psi^{n+1} + \psi^n) = H^n \cdot \frac{\psi^{n+1} + \psi^n}{2}. \quad (\text{A8})$$

Let $t_{n+1/2} = t_n + \Delta t/2$ denote the temporal midpoint and let $\psi_i^* \equiv \psi_i(t_{n+1/2})$ and $H^* \equiv H(t_{n+1/2})$ be the exact wave function and Hamiltonian at this point. Expanding around the midpoint, we have the following:

$$\psi_i^n = \psi_i^* - \frac{\Delta t}{2} \dot{\psi}_i^* + \frac{(\Delta t)^2}{8} \ddot{\psi}_i^* + \mathcal{O}((\Delta t)^3), \quad (\text{A9})$$

$$\psi_i^{n+1} = \psi_i^* + \frac{\Delta t}{2} \dot{\psi}_i^* + \frac{(\Delta t)^2}{8} \ddot{\psi}_i^* + \mathcal{O}((\Delta t)^3), \quad (\text{A10})$$

$$H^n = H^* - \frac{\Delta t}{2} \dot{H}^* + \mathcal{O}((\Delta t)^2), \quad (\text{A11})$$

$$H^{n+1} = H^* + \frac{\Delta t}{2} \dot{H}^* + \mathcal{O}((\Delta t)^2). \quad (\text{A12})$$

From Eqs. (A9)-(A10), the average wavefunction is

$$\frac{\psi^{n+1} + \psi^n}{2} = \psi^* + \frac{(\Delta t)^2}{8} \ddot{\psi}^* + \mathcal{O}((\Delta t)^3). \quad (\text{A13})$$

This remains second-order accurate. Subtracting Eq. (A9) from Eq. (A10), we find:

$$\frac{\psi_i^{n+1} - \psi_i^n}{\Delta t} = \dot{\psi}_i^* + \mathcal{O}((\Delta t)^2). \quad (\text{A14})$$

The Hamiltonian can be decomposed into linear and nonlinear parts:

$$H = H_{\text{linear}} + H_{\text{nonlinear}}, \quad (\text{A15})$$

where H_{linear} contains the hopping terms which are independent of densities and $H_{\text{nonlinear}}$ contains the mean-field and LHY terms. The linear part satisfies $H_{\text{linear}}^n = H_{\text{linear}}^* = H_{\text{linear}}^{n+1}$ exactly. For the nonlinear part, from Eq. (A11):

$$H_{\text{nonlinear}}^n = H_{\text{nonlinear}}^* - \frac{\Delta t}{2} \dot{H}_{\text{nonlinear}}^* + \mathcal{O}((\Delta t)^2). \quad (\text{A16})$$

Inserting this into Eq. (A8), we reach:

$$\begin{aligned} & H^n \cdot \frac{\psi^{n+1} + \psi^n}{2} \\ &= (H_{\text{linear}} + H_{\text{nonlinear}}^* - \frac{\Delta t}{2} \dot{H}_{\text{nonlinear}}^*) (\psi^* + \mathcal{O}((\Delta t)^2)) \\ &+ \mathcal{O}((\Delta t)^2) = H^* \psi^* - \frac{\Delta t}{2} \dot{H}_{\text{nonlinear}}^* \psi^* + \mathcal{O}((\Delta t)^2). \end{aligned} \quad (\text{A17})$$

In particular, the LHY correction $\Delta\mu_1^{\text{LHY}}$ to the chemical potential of the first condensate is a smooth functional of densities n_1 and n_2 :

$$\Delta\mu_1^{\text{LHY}}|_i^n = \mathcal{F}(n_{1,i}^n, n_{2,i}^n; U_1, U_2, U_{12}, m_1, m_2), \quad (\text{A18})$$

where \mathcal{F} denotes the integral over quasi-momentum computed via tanh-sinh quadrature (see Appendix B). The tanh-sinh quadrature evaluates this integral to high precision for given density values; it introduces no time-stepping error since it computes an essentially exact function of its inputs at each instant. Since \mathcal{F} is smooth, we can expand:

$$\begin{aligned} \Delta\mu_1^{\text{LHY}}|_i^n &= \Delta\mu_1^{\text{LHY}}|_i^* - \frac{\Delta t}{2} \left(\frac{\partial \mathcal{F}}{\partial n_1} \dot{n}_{1,i}^* + \frac{\partial \mathcal{F}}{\partial n_2} \dot{n}_{2,i}^* \right) \\ &\quad + \mathcal{O}((\Delta t)^2). \end{aligned} \quad (\text{A19})$$

The exact solution satisfies $i\hbar\dot{\psi}^* = H^*\psi^*$. Comparing the left-hand side of the numerical scheme in Eq. (A6), which is presented in Eq. (A14), with Eq. (A17), which represents the right-hand side of Eq. (A6), we find:

$$i\hbar(\dot{\psi}^* + \mathcal{O}((\Delta t)^2)) = H^*\psi^* - \frac{\Delta t}{2} \dot{H}_{\text{nonlinear}}^* \psi^* + \mathcal{O}((\Delta t)^2). \quad (\text{A20})$$

Using $i\hbar\dot{\psi}^* = H^*\psi^*$, the local truncation error is

$$\tau_{\text{local}} = \frac{\Delta t}{2i\hbar} \dot{H}_{\text{nonlinear}}^* \psi^* + \mathcal{O}((\Delta t)^2) = \mathcal{O}(\Delta t). \quad (\text{A21})$$

The error term $\dot{H}_{\text{nonlinear}}^* \psi^*$ is proportional to the rate of change of the effective potential:

$$\dot{H}_{\text{nonlinear}}^* = U_1 \frac{d|\psi^*|^2}{dt} + U_{12} \frac{d|\phi^*|^2}{dt} + \frac{d\Delta\mu^{\text{LHY}}}{dt}, \quad (\text{A22})$$

where

$$\frac{d|\psi|^2}{dt} = 2 \text{Re}(\psi^* \psi^\dagger) \quad (\text{A23})$$

represents the local probability current. For slowly varying density profiles, such as quasi-equilibrium dynamics, $\dot{H}_{\text{nonlinear}}^*$ is small, and the error is suppressed even though it is formally $\mathcal{O}(\Delta t)$.

For a scheme with local truncation error $\mathcal{O}((\Delta t)^p)$, the global error is typically $\mathcal{O}((\Delta t)^p)$. Thus, the scheme is first-order accurate in time, with the dominant error arising from the nonlinear sector. Despite the reduced temporal accuracy, the semi-implicit scheme retains crucial stability properties [35]. The update can be written as

$$\psi^{n+1} = \left[I + \frac{i\Delta t}{2\hbar} H^n \right]^{-1} \left[I - \frac{i\Delta t}{2\hbar} H^n \right] \psi^n \equiv U^n \psi^n. \quad (\text{A24})$$

When H^n is Hermitian, as is the case for real interaction strengths, the propagator U^n is unitary. Since $(I \pm \frac{i\Delta t}{2\hbar} H^n)^\dagger = (I \mp \frac{i\Delta t}{2\hbar} H^n)$ for the Hermitian H^n , we have

$$(U^n)^\dagger = \left[I + \frac{i\Delta t}{2\hbar} H^n \right] \left[I - \frac{i\Delta t}{2\hbar} H^n \right]^{-1}. \quad (\text{A25})$$

Therefore, $(U^n)^\dagger U^n$ is equivalent to

$$\begin{aligned} &\left[I + \frac{i\Delta t}{2\hbar} H^n \right] \left[I - \frac{i\Delta t}{2\hbar} H^n \right]^{-1} \left[I + \frac{i\Delta t}{2\hbar} H^n \right]^{-1} \\ &\times \left[I - \frac{i\Delta t}{2\hbar} H^n \right] = I, \end{aligned}$$

where in the last step we used that all four matrices commute (as polynomials in H^n) and thus can be rearranged to cancel pairwise. This ensures exact norm conservation:

$$\|\psi^{n+1}\|^2 = \|\psi^n\|^2 \quad (\text{A26})$$

at every time step, regardless of Δt . The scheme is therefore unconditionally stable [36], as no restriction on the timestep is required for numerical stability. This property is essential for long-time simulations of droplet dynamics, where conditionally stable schemes could lead to catastrophic norm growth.

In our simulations, we use $\Delta t = 0.001$ in dimensionless units. Even with formally first-order accuracy in nonlinear terms, the error prefactor $\frac{1}{2} \dot{H}_{\text{nonlinear}}^* \psi^*$ remains small for the parameter regimes studied, where density profiles evolve smoothly. We observe energy conservation to better than 10^{-6} over the full simulation time, confirming that the semi-implicit approximation does not significantly degrade accuracy in practice.

Integration of $\Delta\mu_1^{\text{LHY}}|_i^n$ and $\Delta\mu_2^{\text{LHY}}|_i^n$ is carried out numerically for every lattice site and every timestep using the tanh-sinh quadrature, described in Appendix B.

Appendix B: Tanh-sinh quadrature

Due to the consideration of heteronuclearity in our system, the Lee-Huang-Yang correction to the chemical potential, in Eq. (20), requires numerical evaluation of an integral over quasi-momentum arising from the Bogoliubov spectrum, as no closed-form expression for it exists. In this Appendix, we describe the tanh-sinh quadrature method used for this purpose and justify its suitability for our problem.

The LHY correction of $\Delta\mu_\sigma^{\text{LHY}}$ at each lattice site i involves an integral of the form

$$\Delta\mu_\sigma^{\text{LHY}}|_i = \int_{-K_{\text{max}}}^{K_{\text{max}}} f_\sigma(k; n_{1,i}, n_{2,i}) dk, \quad (\text{B1})$$

where $\sigma \in \{1, 2\}$ labels the condensate component, k is the quasi-momentum, K_{max} defines the Brillouin zone cutoff, and the integrand f_σ depends on the local densities $n_{1,i} = |\psi_i|^2$ and $n_{2,i} = |\phi_i|^2$, which are time-dependent. The integrand arises from the Bogoliubov dispersion relation and is smooth on the open interval $(-K_{\text{max}}, K_{\text{max}})$ and is an even function: $f(-k) = f(k)$. It exhibits a weak integrable cusp near $k = 0$ of the phonon regime, where $f(k) \sim |k|^p$ for some $p > 0$, and it may have large derivatives (endpoint stiffness) near $k = \pm K_{\text{max}}$ due to the finite Brillouin zone cutoff.

Standard quadrature methods such as Gauss-Legendre can struggle with endpoint stiffness [37] and require many nodes

to achieve high accuracy. The tanh-sinh quadrature is specifically designed to handle such integrands efficiently. It was introduced by Takahashi and Mori in 1974 [38], and it belongs to the family of double-exponential methods [39]. The core idea is to transform the integration variable so that the integrand, including any endpoint singularities or stiffness, is mapped to a new function that decays double-exponentially fast, allowing efficient truncation of the integration domain.

We begin by considering a generic integral over the finite region $[-1, 1]$:

$$I = \int_{-1}^1 g(x) dx. \quad (\text{B2})$$

The tanh-sinh transformation introduces a new variable $t \in (-\infty, \infty)$ through

$$x = \varphi(t) \equiv \tanh(c \cdot \sinh(t)), \quad (\text{B3})$$

where c is a constant, conventionally taken to be $c = \pi/2$. The integral becomes

$$I = \int_{-\infty}^{\infty} g(\varphi(t)) \varphi'(t) dt, \quad (\text{B4})$$

with the derivative

$$\varphi'(t) = \frac{c \cosh(t)}{\cosh^2(c \cdot \sinh(t))}. \quad (\text{B5})$$

The key property of this transformation is the asymptotic behavior of $\varphi'(t)$:

$$\varphi'(t) \sim \exp(-c \cdot e^{|t|}) \quad \text{as } |t| \rightarrow \infty. \quad (\text{B6})$$

This double-exponential decay ensures that the transformed integrand $g(\varphi(t)) \varphi'(t)$ vanishes extremely rapidly as $|t| \rightarrow \infty$, even if $g(x)$ has integrable singularities or large derivatives at $x = \pm 1$. Consequently, the infinite integral in Eq. (B4) can be truncated to a finite interval $[-T, T]$ with negligible error for modest values of T .

A complementary perspective is that the transformation concentrates the quadrature nodes near the end points $x = \pm 1$. As $t \rightarrow +\infty$, we have $\varphi(t) \rightarrow 1^-$, and the nodes $x_k = \varphi(t_k)$ cluster densely near $x = 1$. Similarly for $x = -1$ as for $t \rightarrow -\infty$. This dense sampling near endpoints is precisely what is needed to resolve endpoint stiffness or weak singularities.

To apply the tanh-sinh quadrature to Eq. (B1), we first map $k \in [-K_{\max}, K_{\max}]$ to $x \in [-1, 1]$ via the linear transformation

$$k = K_{\max} x, \quad dk = K_{\max} dx. \quad (\text{B7})$$

This gives

$$\Delta\mu_{\sigma}^{\text{LHY}} = K_{\max} \int_{-1}^1 g(x) dx, \quad g(x) \equiv f_{\sigma}(K_{\max}x). \quad (\text{B8})$$

Applying the tanh-sinh transformation presented in Eq. (B3), we find:

$$\Delta\mu_{\sigma}^{\text{LHY}} = K_{\max} \int_{-\infty}^{\infty} g(\varphi(t)) \varphi'(t) dt. \quad (\text{B9})$$

Since $f_{\sigma}(k)$ is an even function, so is $g(x)$. Combined with the oddness of $\varphi(t)$ [i.e. $\varphi(-t) = -\varphi(t)$] and the evenness of $\varphi'(t)$, the integrand in Eq. (B9) is even in t . We can therefore write

$$\Delta\mu_{\sigma}^{\text{LHY}} = 2K_{\max} \int_0^{\infty} g(\varphi(t)) \varphi'(t) dt, \quad (\text{B10})$$

reducing computational effort by half.

The transformed integral is discretized using the trapezoidal rule with uniform step size $h > 0$ on the t -axis:

$$\int_0^{\infty} g(\varphi(t)) \varphi'(t) dt \approx h \sum_{j=0}^N' w_j G_j, \quad (\text{B11})$$

where $t_j = jh$ are the quadrature nodes in the domain t , $x_j = \varphi(t_j)$ are the corresponding nodes in $x \in [0, 1]$, $w_j = \varphi'(t_j)$ are the weights, and $G_j = g(x_j) = f_{\sigma}(K_{\max}x_j)$ are the integrand values. The prime in the summation indicates half the weight in $j = 0$: the term $j = 0$ is multiplied by $1/2$.

The full approximation for the LHY correction is thus

$$\Delta\mu_{\sigma}^{\text{LHY}} \approx 2K_{\max} h \sum_{j=0}^N' w_j G_j. \quad (\text{B12})$$

For integrands that decay double-exponentially, the trapezoidal rule achieves spectral convergence [40], faster than any polynomial. This remarkable property arises because the Euler-Maclaurin error terms, which normally limit the accuracy of trapezoidal peaks, are exponentially small [41] when the integrand and all its derivatives vanish rapidly at the endpoints of integration.

Due to double-exponential decay, shown in Eq. (B6), weights $w_j = \varphi'(t_j)$ become negligibly small for large j . We employ two complementary stopping criteria to determine the truncation point N :

(1) End when the contribution from the j th term falls below an absolute tolerance:

$$K_{\max} h |w_j G_j| < \varepsilon_{\text{abs}}. \quad (\text{B13})$$

(2) End when the partial sum has stabilized to within a relative tolerance:

$$\frac{|S_N - S_{N-1}|}{\max(1, |S_N|)} < \varepsilon_{\text{rel}}, \quad (\text{B14})$$

where $S_N = h \sum_{j=0}^N' w_j G_j$ is the running partial sum. We start with a minimal N and increase until both criteria (1) and (2) are satisfied.

Since nodes $x_j = \varphi(t_j)$ and weights $w_j = \varphi'(t_j)$ depend only on the step size h and the transformation parameter c , which are not part of the integrand, they can be precomputed once at the start of the simulation and reused for every lattice site and every timestep. This significantly reduces computational overhead.

Explicitly, for $j = 0, 1, 2, \dots, N_{\max}$:

$$t_j = jh, \quad (\text{B15})$$

$$x_j = \tanh(c \cdot \sinh(t_j)), \quad (\text{B16})$$

$$w_j = \frac{c \cosh(t_j)}{\cosh^2(c \cdot \sinh(t_j))}. \quad (\text{B17})$$

The total quadrature error has two contributions: (i) the discretization error by approximating the integral by a finite sum and (ii) the truncation error by cutting off the sum at $j = N$ rather than $j = \infty$. Error (i) decreases exponentially with N (for fixed h) or with $1/h$ (for fixed truncation in t), and error (ii) is controlled by the stopping criteria and is typically negligible compared to the discretization error.

For smooth integrands with at most integrable endpoint sin-

gularities, the tanh-sinh method achieves an error that scales as

$$\text{Error} \sim \exp\left(-\frac{c'N}{\log N}\right) \quad (\text{B18})$$

for some constant $c' > 0$.

The Bogoliubov integrand typically behaves as $f(k) \sim |k|$ near $k = 0$ (in the phonon regime), corresponding to an integrable cusp. After the transformation to t , this cusp is mapped to a smooth function at $t = 0$, since $\varphi(0) = 0$ and the cusp is “absorbed” by the transformation. The dense clustering of nodes near $x = \pm 1$ (i.e. $k = \pm K_{\max}$) does not compromise the accuracy at $k = 0$ because the $t = 0$ node sits exactly at $x = 0$ (i.e. $k = 0$), and the smoothness of the integrand away from $k = 0$ ensures rapid convergence.

Pseudocode

The pseudocode presented below summarizes the implementation of the tanh-sinh quadrature for the chemical potential contribution of the LHY correction:

Input: $K_{\max}, h, N_{\max}, \varepsilon_{\text{abs}}, \varepsilon_{\text{rel}}$, density values n_1, n_2 .

Precompute (at the beginning of the simulation):

For $j = 0, 1, \dots, N_{\max}$: compute t_j, x_j, w_j via Eqs. (B16)–(B17).

Evaluate (at each site i for each timestep n):

(a) Initialize: $S \leftarrow 0$.

(b) For $j = 0, 1, \dots, N_{\max}$:

- i. Compute $k_j = K_{\max} x_j$.
- ii. Evaluate $G_j = f_{\sigma}(k_j; n_{1,i}, n_{2,i})$.
- iii. Set $c_j = 1/2$ if $j = 0$, else $c_j = 1$.
- iv. Update: $\Delta S \leftarrow c_j \cdot w_j \cdot G_j; S \leftarrow S + \Delta S$.
- v. If $K_{\max} h |\Delta S| < \varepsilon_{\text{abs}}$ and $|\Delta S| / \max(1, |S|) < \varepsilon_{\text{rel}}$: break.

(c) Return: $\Delta\mu_{\sigma}^{\text{LHY}} = 2K_{\max} h S$.

[1] D. Petrov, Physical Review Letters **115**, 155302 (2015).

[2] H. Kadau, M. Schmitt, M. Wenzel, C. Wink, T. Maier, I. Ferrier-Barbut, and T. Pfau, Nature **530**, 194 (2016).

[3] I. Ferrier-Barbut, H. Kadau, M. Schmitt, M. Wenzel, and T. Pfau, Physical review letters **116**, 215301 (2016).

[4] M. Schmitt, M. Wenzel, F. Böttcher, I. Ferrier-Barbut, and T. Pfau, Nature **539**, 259 (2016).

[5] L. Chomaz, S. Baier, D. Petter, M. Mark, F. Wächtler, L. Santos, and F. Ferlaino, Physical Review X **6**, 041039 (2016).

[6] C. Cabrera, L. Tanzi, J. Sanz, B. Naylor, P. Thomas, P. Cheiney, and L. Tarruell, Science **359**, 301 (2018).

[7] G. Semeghini, G. Ferioli, L. Masi, C. Mazzinghi, L. Wolswijk, F. Minardi, M. Modugno, G. Modugno, M. Inguscio, and M. Fattori, Physical review letters **120**, 235301 (2018).

[8] P. Cheiney, C. Cabrera, J. Sanz, B. Naylor, L. Tanzi, and L. Tarruell, Physical review letters **120**, 135301 (2018).

[9] D. Petrov and G. Astrakharchik, Physical review letters **117**, 100401 (2016).

[10] D. Edler, C. Mishra, F. Wächtler, R. Nath, S. Sinha, and L. Santos, Physical Review Letters **119**, 050403 (2017).

[11] M. Tylutki, G. E. Astrakharchik, B. A. Malomed, and D. S. Petrov, Physical Review A **101**, 051601 (2020).

[12] M. Edmonds, T. Bland, and N. Parker, Journal of Physics Communications **4**, 125008 (2020).

[13] L. Pitaevskii and S. Stringari, *Bose-Einstein condensation and superfluidity*, Vol. 164 (Oxford University Press, 2016).

[14] C. J. Pethick and H. Smith, *Bose-Einstein condensation in dilute gases* (Cambridge university press, 2008).

[15] M. Olshanii, *Physical review letters* **81**, 938 (1998).

[16] V. Dunjko, V. Lorent, and M. Olshanii, *Physical Review Letters* **86**, 5413 (2001).

[17] A. Görlitz, J. Vogels, A. Leanhardt, C. Raman, T. Gustavson, J. Abo-Shaeer, A. Chikkatur, S. Gupta, S. Inouye, T. Rosenband, *et al.*, *Physical review letters* **87**, 130402 (2001).

[18] N. Bogoliubov, *J. Phys* **11**, 23 (1947).

[19] A. L. Fetter and J. D. Walecka, *Quantum theory of many-particle systems* (Courier Corporation, 2012).

[20] F. Dalfovo, S. Giorgini, L. P. Pitaevskii, and S. Stringari, *Reviews of modern physics* **71**, 463 (1999).

[21] P.-G. De Gennes, *Superconductivity of metals and alloys* (CRC press, 2018).

[22] J.-P. Blaizot, G. Ripka, J. W. Negele, H. Orland, and G. E. Brown, “Quantum theory of finite systems and quantum many-particle systems,” (1988).

[23] T. D. Lee, K. Huang, and C. N. Yang, *Physical Review* **106**, 1135 (1957).

[24] E. P. Gross, *Il Nuovo Cimento (1955-1965)* **20**, 454 (1961).

[25] L. P. Pitaevskii, *Sov. Phys. JETP* **13**, 451 (1961).

[26] G. Astrakharchik and B. A. Malomed, *Physical Review A* **98**, 013631 (2018).

[27] I. A. Englezos, P. Schmelcher, and S. I. Mistakidis, *SciPost Physics* **19**, 133 (2025).

[28] J. Crank and P. Nicolson, in *Mathematical proceedings of the Cambridge philosophical society*, Vol. 43 (Cambridge University Press, 1947) pp. 50–67.

[29] W. H. Press, S. A. Teukolsky, W. T. Vetterling, and B. P. Flannery, Cambridge: New York (2007).

[30] B. Weizhu, D. Jaksch, and P. A. Markowich, *Journal of Computational Physics* **187** (2003).

[31] X. Antoine, W. Bao, and C. Besse, *Computer Physics Communications* **184**, 2621 (2013).

[32] J.-M. Sanz-Serna and M.-P. Calvo, *Numerical hamiltonian problems*, Vol. 7 (Courier Dover Publications, 2018).

[33] L. H. Thomas, *Watson Sci. Comput. Lab. Rept.*, Columbia University, New York **1**, 71 (1949).

[34] G. Golub and C. Van Loan, Baltimore, MD (2013).

[35] M. Caliari, C. Neuhauser, and M. Thalhammer, *J. Comput. Phys* **228**, 822 (2009).

[36] W. Bao and Q. Du, *SIAM Journal on Scientific Computing* **25**, 1674 (2004).

[37] P. J. Davis and P. Rabinowitz, *Methods of numerical integration* (Courier Corporation, 2007).

[38] H. Takahasi and M. Mori, *Publications of the Research Institute for Mathematical Sciences* **9**, 721 (1974).

[39] M. Mori and M. Sugihara, *Journal of Computational and Applied Mathematics* **127**, 287 (2001).

[40] D. H. Bailey, K. Jeyabalan, and X. S. Li, *Experimental Mathematics* **14**, 317 (2005).

[41] L. N. Trefethen and J. Weideman, *SIAM review* **56**, 385 (2014).